ORIGINAL RESEARCH ARTICLE

Characterization and Fracture Behavior of ZrC-ZrSi$_2$-Al$_2$O$_3$ Composite Coating with Densely Packed Whiskers Microstructure Prepared by Atmospheric Plasma Spraying

Yu-xuan Shao[1] · Yong Yang[1,3] · Hao-en Liang[1] · Ce-ce Zhao[1] · Wei Tian[2]

Abstract A ZrC-ZrSi$_2$-Al$_2$O$_3$ powder system was designed and used for preparing ZrC composite coating. Tailored microstructures such as densely packed ZrC-ZrSi$_2$ whiskers and nanosized alumina grains were observed in the coating lamellae. The zirconia derived from the oxidation of zirconium carbide and zirconium silicide during the plasma spraying process contributed to the formation of the near-eutectic alumina-zirconia area. The formation mechanism of the composite coating was discussed based on the characterization of the coating lamellae and the as-prepared coating demonstrated promising mechanical properties due to the coordination of whiskers and eutectic microstructure.

Keywords atmospheric plasma spraying · fracture behavior · whiskers · ZrC composite coating

✉ Yong Yang
yangyonghebut@163.com; yangyong@hebut.edu.cn

1 Key Lab. for New Type of Functional Materials in Hebei Province, School of Materials Science and Engineering, State Key Laboratory of Reliability and Intelligence of Electrical Equipment, Tianjin Key Laboratory of Materials Laminating Fabrication and Interface Control Technology, Hebei University of Technology, Tianjin 300132, People's Republic of China

2 AECC Sichuan Gas Turbine Establishment, Chengdu 610500, Sichuan Province, People's Republic of China

3 Tianjin, People's Republic of China

Introduction

Critical components in aircraft like the leading edge and the sealing part are facing thermal-mechanical coupling service conditions. And preparing coatings with favorable properties on the surface of these metal/light-weight materials (like C$_f$/C composites) made sections could be a straight forward way for protecting them from failure (Ref. 1). Zirconium carbide (ZrC) is featured with high microhardness (27 GPa), ultra-high melting point (3580 °C), and relatively low density (Ref. 2, 3), while monophase ZrC coating shows substantial brittleness at room temperature and a porous zirconia layer is prone to be formed on the coating surface under high-temperature oxidative atmosphere (Ref. 4). Therefore, modifications are welcomed to be made in order to elevate the mechanical and high-temperature properties at the same time and more importantly, build a wider application for ZrC coating.

Al$_2$O$_3$ is a widely used coating material and it has been well-investigated in massive works. The well-suited properties combination of zirconium carbide and alumina has been validated by many works, including composites and coatings. Al$_2$O$_3$-ZrC composites were fabricated by hot-pressure sintering in the early work by Zambetakis et al. (Ref. 5). It is revealed that the composites have better toughness and strength than the pure alumina bulks. Yeh et al. (Ref. 6) validated the feasibility of fabricating ZrC-Al$_2$O$_3$ composites and powders via the combustion reactions in the ZrO$_2$/Al/C system. A step forward, the WC/ZrC/Al$_2$O$_3$ powders were synthesized by combustion reactions in WO$_3$/ZrO$_2$/Al/C system (Ref. 7). For high-temperature applications, recent works by Huo et al. (Ref. 8) highlighted the positive effect of alumina on the ablation-resistant property of ZrC composite coatings. It was found that compact Al-Zr-O grains formed during the ablation process could effectively prevent the inner coating from hot corrosion. Moreover, it was worth

noting that the addition of silicides like SiC (Ref. 9, 10), $MoSi_2$ (Ref. 11), and $ZrSi_2$ (Ref. 12) could also improve the high-temperature properties of ZrC and ZrB_2 composite coating. A SiC-ZrC-Al_2O_3 anti-ablation coating was prepared by Huo et al. (Ref. 13), and it was found that dense Zr-Si-O and Zr-O-Al-Si layer formed on the coating surface also do great help for elevating the ablation properties of the mono- phase coating. Therefore, it is believed that the composite coating with the combination of ZrC, Al_2O_3, and silicides could have promising mechanical and high-temperature properties.

In this work, a ZrC-$ZrSi_2$-Al_2O_3 composite coating was designed and then prepared by high-efficient atmospheric plasma spraying. Densely packed ZrC-$ZrSi_2$ whiskers are found in the as-prepared coating. Although the interaction between oxygen and zirconium carbide in the atmosphere is inevitable, the zirconia formed in the preparation process contributed to the formation of near-eutectic alumina-zirconia microstructure in the final coating and this could be an effective way for the regulation of the zirconia inclusions. These tailored and intriguing microstructural characteristics, which have the positive effect on enhancing the mechanical properties, have not been reported in the previous works with similar coating compositions. The formation mechanism, fracture behavior of the ZrC-$ZrSi_2$ whiskers, and the mechanical properties of the composite coating were fully investigated and discussed.

Experimental Details

Powder Preparation

Commercially available ZrC (purity: 99.9%, 1-3 μm), $ZrSi_2$ (purity: 99.9%, $\sim$ 5 μm), Al_2O_3 (purity: 99.9%, $\sim$ 0.04 μm) were used as the start materials following the mass ratios of 37:28:35. The ratio for dispersant (sodium polyphosphate) and adhesive (sodium hydroxymethyl cellulose) is 1:50. The mixture of raw material powders, deionized water, dispersant, and adhesive was selected for preparing composite powders by spraying granulation method. The homogenous mixture obtained by centrifugal stirring lasted for 2 h and was pumped into the atomizer by a peristaltic pump (rotation speed: 35 r/min, $\sim$ 120 ml/min). The moisture in the mixed drops underwent rapid evaporation in the heating zone (heating temperature: $\sim$ 230 °C). At the same time, the adhesive solidified quickly and the spherical composite powders were prepared. An overall SEM image of the as-prepared powders is randomly selected and captured (magnification: 100 x, about 500 particles in the field). The size of each powder in this image was measured and recorded to obtain the final particle size distribution of the spray-drying prepared powders.

Coating Preparation

Titanium alloy (Ti6Al4V) was used as the substrate (10 mm × 10 mm × 12 mm). Substrates were finely grit-blasted to obtain desired roughness before plasma spraying (Quartz sand, sandblasting distance: 100-150 mm, sandblasting angle: 70-80°, surface roughness of the blasted surface (Ra): 8-10 μm). NiCrAlY was used as the bonding layer. The coatings were prepared by a GP-80 type plasma spraying system (Jiujiang Spraying Equipment Co., Ltd., China). Several substrates are placed in a row and then fixed vertically to the torch initiation direction. Then the plasma gun with powder injection was moved under a reciprocate route (a rectangle path around the substrates) with a speed of about 120 mm/s. And this route was repeated 5 times (one detour is regarded as one time) to prepare the composite coating with a thickness value higher than 200 μm. The spraying parameters adopted in this work are as follows: (a) Primary gas (Ar) flow rate: 1.33 L/s, (b) Secondary gas (H_2) flow rate: 0.33 L/s, (c) Powder flow rate: 0.15 g/s, (d) Power: $\sim$ 35 kW, (e) Spraying distance: $\sim$ 100 mm.

Characterization and Test

X-ray diffraction (XRD, Rigaku DMAX-2500 with Cu Kα radiation, Japan) was adopted at 30 kV for measuring the phase composition of the powders and coatings. The spectrum was collected in the 2θ range of 20 $\sim$ 80° with a step length of 0.02°. Scanning electron microscope (Hitachi S-4800 and JSM-6510A, both equipped with EDS) was used to demonstrate the morphology of the powders and the microstructures of the coatings. Indentation tests for 20 times were conducted on the polished coating surface by a micro-Vickers hardness tester (SHIMADZU HMV-2, load: 0.98 N, loading time: 15 s, 20 times) with Vickers pyramid shape diamond indenter. The fracture toughness of the composite coating was measured (load: 4.9 N, loading time: 15 s, 10 times) and calculated by the formula as follows (Ref. 14):

$$K_{IC} = P\left(\pi\left(\frac{C_1 + C_2}{4}\right)\right)^{-\frac{3}{2}}\tan^{-1}\beta \qquad \text{(Eq 1)}$$

Results and Discussion

Characterization of Spray Drying Prepared Powders and As-Prepared Coating

The overall profile and detailed microstructure of the surface of the ZrC-$ZrSi_2$-Al_2O_3 composite powder are shown in Fig. 1(a) and (b). Optimal mixture and compact bonding

of the start materials were obtained by the spray drying method and the flowability of the start materials was elevated. It is shown in Fig. 1(d) that the particle size of the composite powders is mainly located in the range of 40-60 μm.

The XRD patterns of the ZrC-ZrSi$_2$-Al$_2$O$_3$ composite powder and the powder-derived coating are shown in Fig. 2. The major phases of the as-prepared composite coating were ZrC, ZrSi$_2$, and Al$_2$O$_3$. Meanwhile, the oxidation of the coating composition result in the inclusion of oxides like zirconia and silica. Rietveld refinement method was used to conduct full-spectrum fitting of the XRD patterns of the coating. It was calculated that the content values for tetragonal zirconia and monoclinic zirconia were 7.660 wt.% and 3.565 wt.%, respectively. Moreover, the phase content values for ZrC and ZrSi$_2$ were 31.012 wt.% and 24.399 wt.%, respectively. Compared to the content values of the phases in the composite powders, it could be inferred that zirconium carbide underwent more severe oxidation than zirconium silicide during the atmospheric plasma spraying process. Zirconium carbide is prone to be oxidized in the atmosphere when the ambient temperature is higher than 400 °C due to its higher affinity with oxygen. And the oxidation of ZrC could be considered as two steps (Ref. 15): (i) the ZrC phase reacts with oxygen to form zirconia and carbon; (ii) the carbon is set free and reacts with the penetrating oxygen. The zirconia layer on the surface of the particle is porous, while it is revealed by Zhu et al. (Ref. 16) that the zirconium silicide phase will be oxidized gradually in the atmosphere in the temperature range of 600-700 °C with obvious mass gain. It is postulated that for the ZrSi$_2$ feedstock, a SiO$_2$ layer could be formed on the particle surface when it interacts with oxygen in the plasma jet. And this oxide layer further prevents the invasion of oxygen into the inner part of the particle. Generally, ZrC and ZrSi$_2$ phases maintained desired phase stability during the plasma spraying process and ZrC-ZrSi$_2$-Al$_2$O$_3$ composite coating was successfully prepared.

The SEM image of the polished coating cross section of the as-prepared ZrC-ZrSi$_2$-Al$_2$O$_3$ composite coating is demonstrated in Fig. 3(a). The thickness value of the
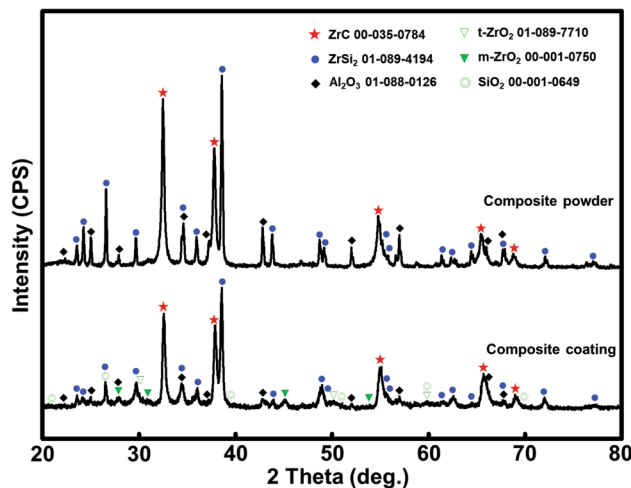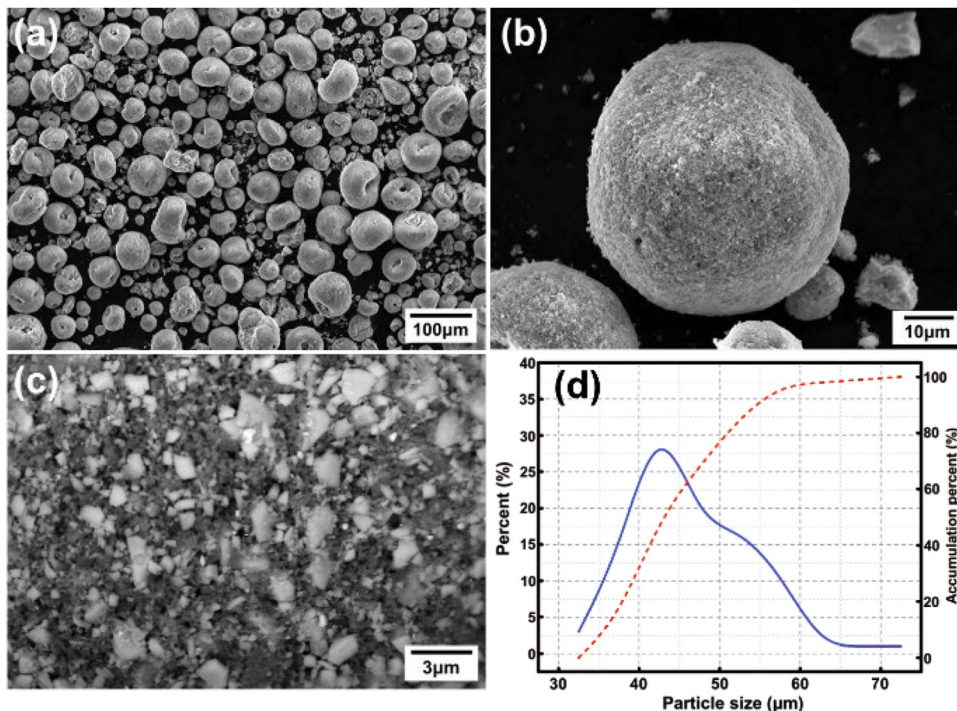

Fig. 2 XRD patterns for the as-prepared composite powder and composite coating.

Fig. 1 Characterization of the spherical composite powders prepared by spray drying: (a) SEM image of the overall profile of the powder, (b) SEM image of a single composite powder, (c) SEM image of the magnified powder surface, (d) Particle size information of the composite powders.

coating is about 200 μm and the typical lamellar structure could be observed. Different contrasts shown on the BSE image (Fig. 3(b)) could be classified by distinctive microstructural characteristics and the possible phases contained in the marked areas may be able to be clarified by the phase identification results in Fig. 2 and EDS results in Table 1: (i) The lamella marked by A, which is mainly composed of element Zr, Si and C, could be characterized as densely packed $ZrC-ZrSi_2$ whiskers. (ii) The lamella marked by B was rich in elements Al and O, referring to the alumina-rich lamella. This kind of lamella shows light contrast in the SE image (Fig. 3(a)) due to the surface charging effect caused by the reflection of the secondary electron and its real contrast could be identified by the BSE image. (iii) The lamella marked by C may mainly be composed of $ZrSi_2$ and ZrC phases. And some zirconia may involve in the lamella considering the higher content of element O of this area compared to area A. Correspondingly, this kind of lamella shows the lightest contrast in the BSE image. (iv) The lamella marked by D mainly contains elements Al, Zr, and O while elements C and Si can hardly be detected. It is worth noting that, even though the content values of elements Al, Zr, and O were similar to area B (content for element Zr was lower), this kind of lamella (D) shows some kind of near-eutectic microstructure (will be mentioned in the following discussion). To sum up, the start materials showed desirable melting during the plasma spraying process and there were few unmelted feedstocks. Compact interlamellar bonding was observed and few pores and cracks could be found. Based on the analysis above, these aforementioned microstructures are further characterized and discussed.

Lamellae containing ZrC and $ZrSi_2$ whiskers are fully characterized in Fig. 4. Generally, it could be concluded that the whiskers were closely arranged with dense microstructure (as shown in Fig. 4a, b, and c), while it could be found that the whiskers in the coating lamellae demonstrated different morphologies such as lath-like microstructure (area A in Fig. 4a), closely knitted microstructure (area B in Fig. 4a), and dendrites-like microstructure (area C in Fig. 4b). The solidification process of a high-temperature droplet derived from the plasma spraying process could be non-equilibrium and the eventually formed microstructure is affected by the undercooling condition and local phase contents in the droplets. Element C can hardly be detected in area A and it could be known that the lath-like microstructure was mainly composed of $ZrSi_2$. Higher content of element C was detected in the dendrites-like microstructure (area C) compared to closely knitted whiskers (area B).

It could be seen in the SEM image of the coating fracture surface (Fig. 4c) that the lamella composed of closely-knitted $ZrC-ZrSi_2$ whiskers demonstrated three-dimensional networks microstructure. Good integrity of the whiskers could be observed on the fracture surface and intimate bonding between the adjacent lamellae was obtained, indicating desirable cohesion of the lamella. The co-existence of fine grains and whiskers was shown in Fig. 4(b). Dendrites branching from the primary crystal (shown in Fig. 4(d), magnified image of the area marked by the yellow rectangle in (b)) were characterized with dense microstructure. It was believed that densely packed whiskers (also shown in the upper half of Fig. 4d) could be formed under sufficient arborescent crystalline growth (primary crystal and branching dendrites).

Under the rapid heating of the plasma jet, the melts derived from different phases possessed varied viscosity, leading to the localization of different phases to a greater or lesser extent. Therefore, phase detachment could occur during the deposition process of the droplets with localized

Table 1 EDS results of the marked areas in Fig. 3 (b)

Element	Zr, wt.%	Al, wt.%	O, wt.%	C, wt.%	Si, wt.%
A	50.85	0.09	0.46	7.67	40.93
B	8.77	47.77	37.59	5.48	0.38
C	51.45	5.08	4.49	6.99	31.98
D	7.52	54.70	37.78	…	…

Fig. 3 Cross-sectional microstructure of the ZrC-$ZrSi_2$-Al_2O_3 composite coating: (a) Overall SEM image, (b) Typical back scattered electron image
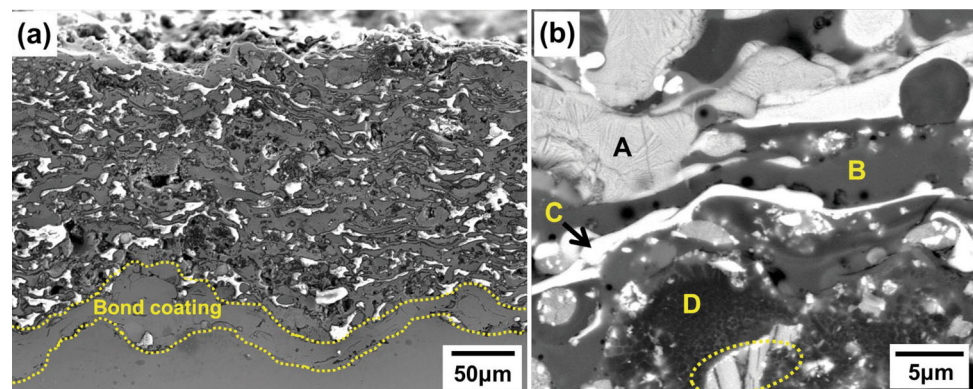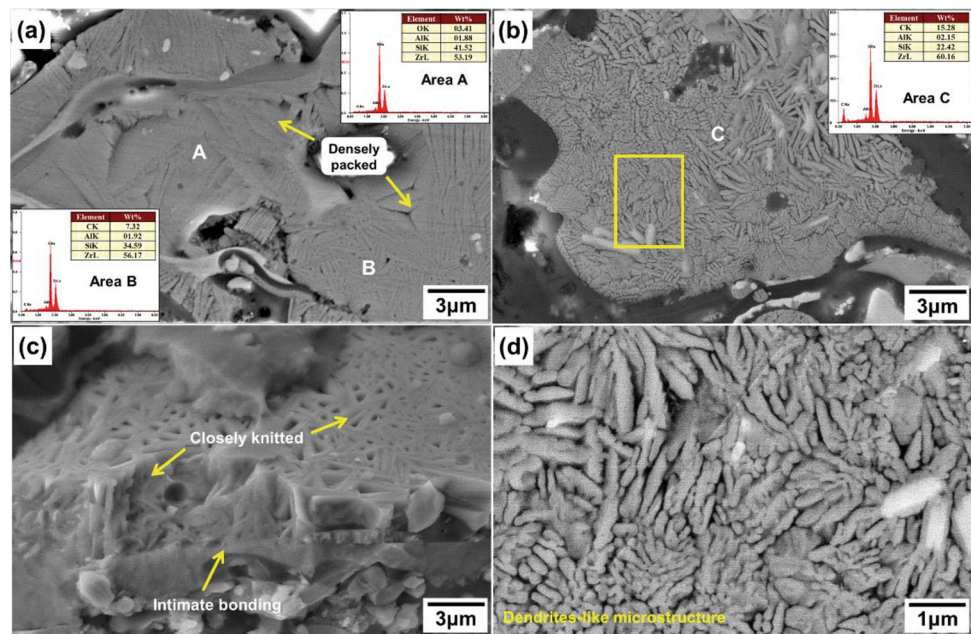
Fig. 4 SEM images of the ZrC-ZrSi$_2$ whiskers: (a) for polished coating cross section, (b) for polished coating surface, (c) for a three-dimensional view of the densely packed whiskers, (d) for the magnified image of the marked area in (b).

phases and eventually result in the distribution of the microstructures with different morphologies. Regardless of other factors such as undercooling or nucleation form (heterogeneous nucleation or what), it could be inferred that the densely packed whiskers microstructure could be formed only when the zirconium carbide accounted for a certain volume in the ZrC-ZrSi$_2$ system. Moreover, the solidified microstructure of this system tends to be like dendrites when the ZrC component reaches a higher percentage.

Alumina-rich lamellae were characterized with dark contrast and seemingly featureless microstructure (like area B in Fig. 3b). While the detailed characterization of the coating fracture surface demonstrated that this kind of lamellae was composed of nanosized alumina grains (as shown in Fig. 5). Nanosized alumina feedstock was melted or sintered with each other under the high-temperature plasma jet during the plasma spraying process and sintering neck could be found in Fig. 5(b). The microstructural characteristic of the alumina-rich lamellae could be summarized as fully melted alumina solidified as the substrate with nanosized alumina grains embedded in it.

Zirconia formed during the plasma spraying process was mainly tetragonal phases in the as-prepared ZrC composite coating. Traditionally, the reason for pure zirconia (without stabilization like YO$_{1.5}$ or CeO$_2$) keeping in this meta-stable phase after the rapid cooling process could be described as two aspects. For one, it was argued that tetragonal zirconia could keep at room temperature when the grain size of the as-formed zirconia phase was lower than its intrinsic critical grain size (about 40 nm). For

another, during the cooling process, the volume expansion of the zirconia particles, which was caused by the phase transformation from tetragonal to monoclinic, might be inhibited by the high stress level around them. And therefore, this meta-stable phase could be kept until the stress was released (Ref. 17).

It could be known from the phase diagram of the zirconia-alumina system that the optimal eutectic point for these two components was: Al$_2$O$_3$ (63 mol.%)-ZrO$_2$ (37 mol.%) (Ref. 18). While considering the smaller contents of zirconia in the as-prepared composite coating, it was believed that the microstructure with lean zirconia content could be formed, which could also be verified by the EDS results in Fig. 6(a). The zirconia-leaned microstructure shown in Fig. 6(b) contained lath-like or spherical alumina primary phase with zirconia distributed on the boundaries. It was postulated that the compact bonding of the alumina particles in this microstructure inhibited the volume expansion of the tetragonal zirconia phase and then a dense near-eutectic alumina-zirconia microstructure was formed. Good compatibility between the eutectic microstructure and whiskers could be found in Fig. 6(a) and from a magnified perspective (Fig. 6c), these two microstructures demonstrated compact interlocks.

Formation Mechanism of the ZrC-ZrSi$_2$ Whiskers in the Coating Lamellae

Whiskers, spherical and rod-like particles were the common microstructures formed for zirconium carbide after the solidification of the high-temperature liquid phase (Ref.

Fig. 5 Characterization of the typical Al-O rich lamellae embedded with nanosized alumina grains: (a) for overall morphology, (b) for detailed characterization.
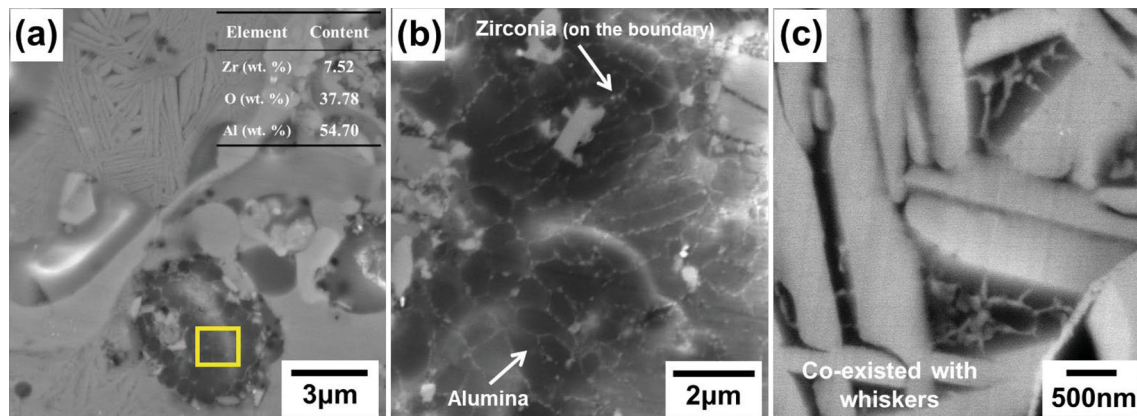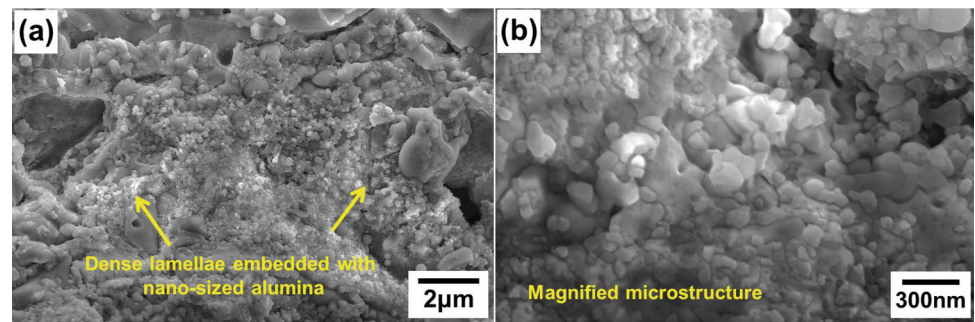

Fig. 6 Characterization of near-eutectic alumina-zirconia microstructure in the ZrC-ZrSi$_2$-Al$_2$O$_3$ composite coating: (a) for the area with the co-existence of densely packed whiskers and near-eutectic microstructure, (b) for the detailed characterization of the near-eutectic, (c) the interlock distribution of the whiskers and near-eutectic.

19, 20). The formation mechanism of the ZrC whiskers reported in the former works could be summarized as "the whiskers precipitated from the melt or the precursor and then grew with certain preference (Ref. 19, 21, 22)." Dendrites and whiskers with similar microstructure for zirconium carbide are also reported in works on preparing ZrC composite bulk materials by arc melting method (Ref. 23, 24). That is to say, the premise for the formation of the whiskers in the composite coating was the desirable melting of the zirconium carbide. The results presented in the former section support the idea that the zirconium carbide could be fully melted by adopting ZrC-ZrSi$_2$-Al$_2$O$_3$ composite powder system to atmospheric plasma spraying.

The discussion was focused on the formation mechanism of the ZrC-ZrSi$_2$ whiskers in the coating lamellae. Unlike the lamella composed of merged ZrC, ZrSi$_2$, and alumina (like the area marked by a yellow circle in Fig. 7b), a clear interface could be observed between the whiskers-contained lamella and the alumina-rich lamella in Fig. 7(a). Therefore, it could be inferred that the solidification of the alumina-rich lamella was prior to the whiskers-contained lamella (Ref. 25). Rod-like fine grains (marked by the blue triangles in Fig. 7) could be observed in the area adjacent to the solidified lamella below. While it could be distinguished that the grains above the

aforementioned fine-grained area transformed into the typical whiskers with certain aspect ratios. The similar microstructure could also be observed in Fig. 4(b).

Melt-solidification was one of the basic ideas for the fabrication of bulk and coating materials. Nevertheless, unlike the controllable solidification process in the arc-melting method, the solidification process for the droplets derived from plasma heating could be extremely non-equilibrium. Moreover, the spreading and solidification processes were affected by the temperature of the droplets and the adjacent lamellae. While two points could be assured: (i) The solidification of the former splat was prior to the splash of the latter droplets; (ii) For an after-spreading droplet, the main solidification direction of the droplet was vertical to the spreading direction (Ref. 25, 26). The formation mechanism of the ZrC-ZrSi$_2$ whiskers in the coating lamellae derived from the all-inclusive microstructure characterizations was summarized in the schematic graphs in Fig. 8. A fully melted droplet containing ZrC, ZrSi$_2$, and Al$_2$O$_3$ phases splashed on the previously formed splat and then spread on it. There was an obvious temperature gradient from the interface along the splats to the surface of the spread droplet. And the undercooling degree becomes higher in this direction. Comparable to the formation process of the alloy castings, the

Fig. 7 Observation of the typical lamellae containing ZrC-ZrSi$_2$ whiskers (on the polished coating cross section) (a) For overall characterization, and (b) for local observation.
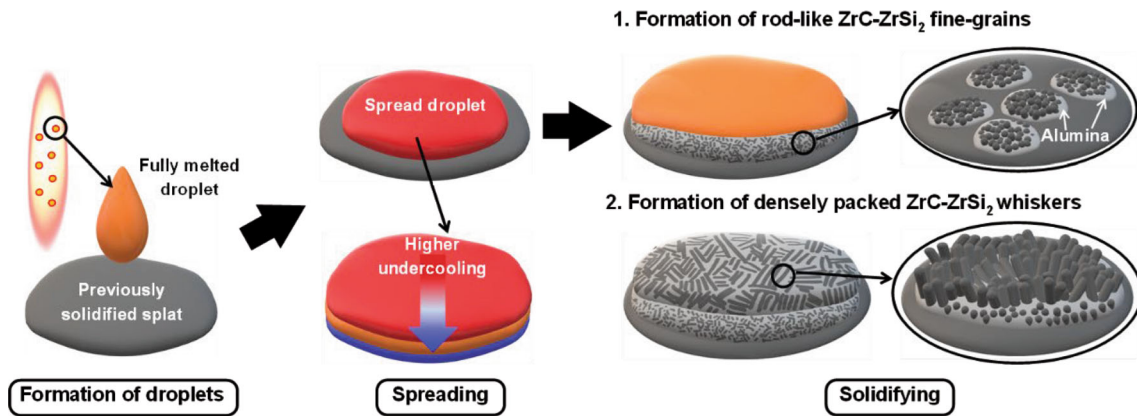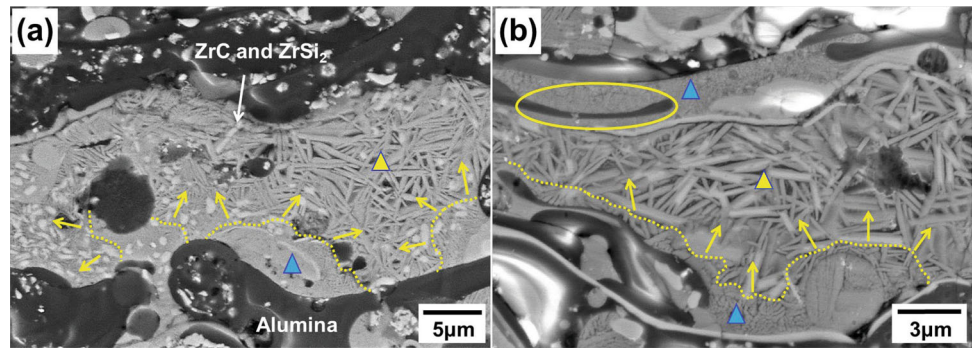

Fig. 8 Schematic graph of the formation mechanism of the densely packed ZrC-ZrSi$_2$ whiskers.

previously deposited splat (composed of nanosized alumina) could be the matrix for heterogeneous nucleation. Higher undercooling degrees along the interface between the high-temperature liquid phase and solidified splat contributed to the formation of the rod-like fine grains (as shown in Fig. 4b and the areas marked by blue triangles in Fig. 7b). While the undercooling degree for the liquid phase far away from the previously deposited splat could be lower and the ZrC and ZrSi$_2$ phases nucleated and underwent further grain growth along the preferred direction ((111) for ZrC and (131) for ZrSi$_2$) based on the formed fine-grains. Eventually, the ZrC-ZrSi$_2$ whiskers with certain aspect ratios were formed.

Mechanical Properties of ZrC-ZrSi$_2$-Al$_2$O$_3$ Composite Coating

Results for Microhardness and Fracture Toughness

Weibull distribution of the microhardness of the ZrC composite coating prepared by atmospheric plasma spraying ZrC-ZrSi$_2$-Al$_2$O$_3$ composite powder is shown in Fig. 9. The average microhardness of the as-prepared composite coating was 1039 HV$_{0.1}$ and the maximum value was 1289 HV$_{0.1}$. Furthermore, the microhardness values of the APS-prepared coatings with similar coating compositions were
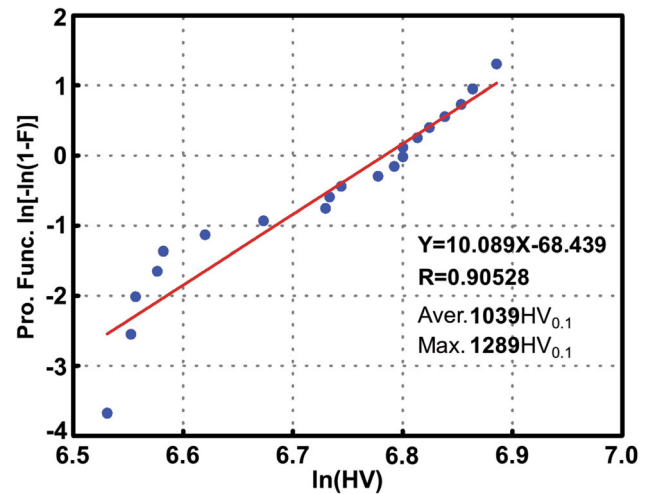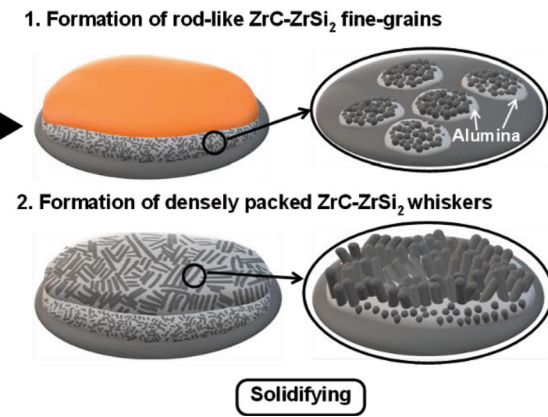

Fig. 9 Weibull distribution of the microhardness value of the ZrC-ZrSi$_2$-Al$_2$O$_3$ composite coating.

listed in Table 2 for a fair comparison. It should be noted that although zirconium carbide and alumina were characterized with high microhardness, the intrinsic hardness for zirconium silicide was relatively low (about 1060 HV). It could be known from Table 2 that the microhardness value of the as-prepared composite coating was higher than that of the ZrC or TiC reinforced cement coatings, similar to the microhardness value of the TiC and TiB$_2$ reinforced

Table 2 Comparation of the microhardness of the APS prepared composite coatings reported in recent years.

Coating system	Preparation method	Microhardness	Refs.
ZrC-ZrB_2/Ni	Atmospheric plasma spraying	525 $HV_{0.1}$	Ref. [27]
TiC-TiB_2-60NiAl	Atmospheric plasma spraying (SHS)	915 HV	Ref. [28]
TiB_2-TiC-Co	Atmospheric plasma spraying (SHS)	1059 HV	Ref. [29]
TiC	Atmospheric plasma spraying	784 $HV_{0.2}$	Ref. [30]
TiC-Ti_5Si_3	Atmospheric plasma spraying (Reactive synthesis)	> 1000HV	Ref. [31]
ZrB_2-ZrC-SiC	Atmospheric plasma spraying (Reactive synthesis)	990 $HV_{0.1}$	Ref. [32]
ZrB_2-ZrC	Atmospheric plasma spraying (Reactive synthesis)	1185 $HV_{0.1}$	Ref. [33]
Al_2O_3-30wt%TiB_2	Atmospheric plasma spraying	1145 HV	Ref. [34]
ZrC-$ZrSi_2$-Al_2O_3	Atmospheric plasma spraying	1039 $HV_{0.1}$(Max. 1289 $HV_{0.1}$)	This work

cobalt hard coatings. For APS-prepared ceramic composite coatings, the microhardness value of the coating prepared in this work was higher than that of the TiC single-phase coating, reactively synthesized TiC-Ti_5Si_3 composite coating and ZrB_2-ZrC-SiC composite coating, similar to the microhardness value of the TiB_2 reinforced alumina composite coating, lower than the microhardness value of reactively synthesized ZrB_2-ZrC composite coating.

The fracture behavior of the as-prepared ZrC composite coating was observed and analyzed based on the surface indentation morphology. And it was calculated that the average fracture toughness of the composite coating was 3.30 $MPa/m^{1/2}$. Figure 10(a) demonstrates the overall morphology of the indentation. It could be found that both the area composed of densely packed whiskers and the area rich in alumina showed dense microstructure. The cracks are prone to initiate and propagate from the indentation tip (marked by a yellow circle in Fig. 10a) and the area with gas entrapment (the area on the left of the indentation). Obvious crack branching could be found along the crack propagation path that existed in the whiskers-contained microstructure.

Figure 10(b), (c), and (d) displays the crack propagation path under different magnifications. Both inter-granular fractures and trans-granular fractures could be observed on the propagation path. The existence of whiskers leads to obvious crack deflections and zigzag propagation path (marked by yellow circles in Fig. 10b, c, and d). The trans-granular fracture of the whiskers (Fig. 10c) could greatly elevate the energy consumption during the propagation process. And it should be mentioned that obvious deflection (shown in Fig. 10b) could be found around the area containing near-eutectic alumina-zirconia microstructure (point by arrows in Fig. 10b) and whiskers (also mentioned in Fig. 6c). Crack deflection in a smaller scale could be observed in Fig. 10(d) (marked by a blue circle) and finally, the crack propagation ended in the densely packed whiskers.

Strengthening and Toughening Mechanism of the Composite Coating

Problems caused by the substantial and intrinsic brittleness of ceramic materials could be solved by introducing special microstructures. Specifically, the proportion of pores and interlamellar cracks could also affect the mechanical properties of the plasma-spraying prepared ceramic coatings. For one, whiskers and rod-like grains could effectively prolong the crack propagation path by causing obvious crack deflection and then inhibiting the propagation. Moreover, the intrinsic strength of zirconium carbide was high, which could greatly contribute to the toughening of ceramics (Ref. [19], [35]). For another, lamellae containing whiskers, closely arranged alumina, and alumina-zirconia eutectic contributed to the densification of the composite coating. In summary, the strengthening and toughening mechanism of the as-prepared ZrC composite coating could be ascribed to the following points from a microstructural perspective:

(i) Toughening effect of the whiskers. ZrC-$ZrSi_2$ whiskers in the coating lamellae formed a strong and three-dimensional network microstructure (as shown in Fig. 4c). Cracks not only propagated along the coating surface but also deep inside the coating lamellae. Closely knitted whiskers greatly improved the toughness of the composite coating.

(ii) Strengthening effect of the alumina-rich microstructure. For one, the alumina lamella itself kept a dense and fine-grained microstructure; For another, the formation of near-eutectic alumina-zirconia microstructure greatly offset the negative effect brought by the inclusion of the zirconia. More importantly, the alumina-rich lamella acted as the matrix for the heterogeneous nucleation of ZrC and $ZrSi_2$ liquid phases and then facilitate the formation of whiskers microstructures.

Fig. 10 Fracture behavior of the ZrC-ZrSi$_2$ whiskers by observing the surface indentation: (a) for the SEM images of a typical indentation, (b)-(d) were the SEM images of the crack propagation path located on the crack initiation section, middle of the propagation path and end of the propagation path, respectively.
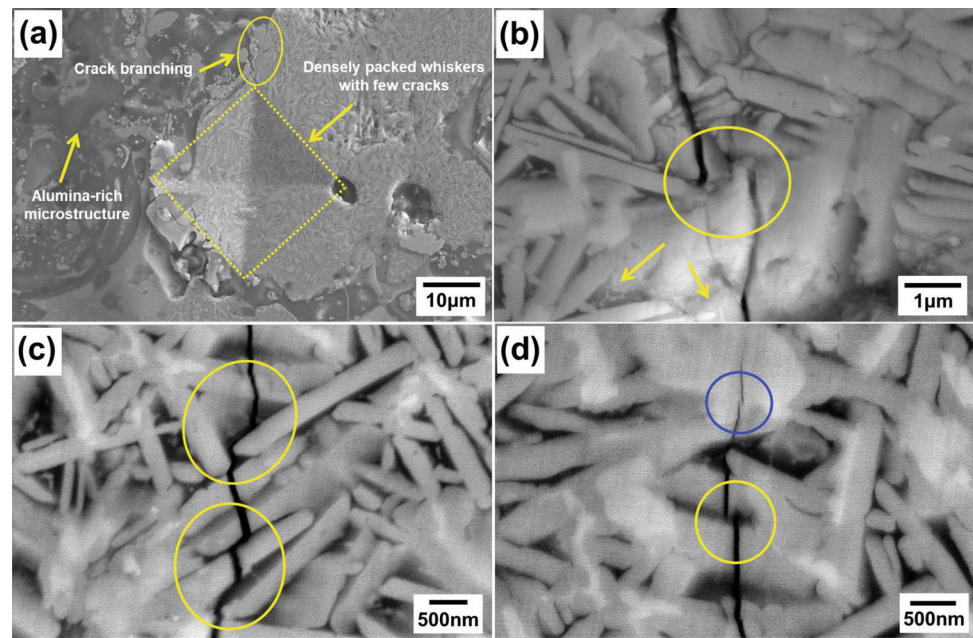
Conclusions

a. Spherical ZrC-ZrSi$_2$-Al$_2$O$_3$ composite powder was designed, prepared, and used for atmospheric plasma spraying to prepare a ZrC composite coating with dense microstructure.

b. Desirable melting of the refractory zirconium carbide feedstocks was obtained. Compactly bonded lamellae containing densely packed ZrC-ZrSi$_2$ whiskers, nano-sized alumina grains, and alumina-zirconia eutectic microstructure were observed in the as-prepared composite coating.

c. The formation of the whiskers-contained lamellae could be summarized as: After the spreading of the droplets, the liquid phase near the splat interface solidified as rod-like fine grains first, and then the whiskers were formed in the upper liquid phase following the preferred orientation of each phase.

d. Crack deflection caused by the whiskers, the trans-granular fracture of the whiskers, and the cooperation between the whiskers and alumina-zirconia eutectic microstructure brought promising mechanical properties of the composite coating.

Data availability The raw/processed data required to reproduce these findings cannot be shared at this time as the data also form part of an ongoing study.

References

1. M. Natali, J. Kenny and L. Torre, Science and Technology of Polymeric Ablative Materials for Thermal Protection Systems and Propulsion Devices: A Review, *Prog. Mater. Sci.*, 2016, **84**, p 192-275.

2. B.R. Golla, A. Mukhopadhyay, B. Basu and S.K. Thimmappa, Review on Ultra-High Temperature Boride Ceramics, *Prog. Mater. Sci.*, 2020, **111**, p 100651.

3. D. Ni, Y. Cheng, J. Zhang, J. Liu, J. Zou, B. Chen, H. Wu, H. Li, S. Dong, J. Han, X. Zhang, Q. Fu and G. Zhang, Advances in Ultra-High Temperature Ceramics, Composites, and Coatings, *J. Adv. Ceram.*, 2021, **11**, p 1-56.

4. X. Pan, Y. Niu, T. Liu, X. Zhong, C. Li, M. Shi, X. Zheng and C. Ding, Ablation Resistance and Mechanism of ZrC-SiC-Yb$_2$O$_3$ Ternary Composite Coatings Fabricated by Vacuum Plasma Spray, *J. Eur. Ceram. Soc.*, 2019, **39**, p 3604-3612.

5. T. Zambetakis, J.L. Guille, B. Willer and M. Daire, Mechanical Properties of Pressure Sintered Al$_2$O$_3$-ZrC Composites, *J. Mater. Sci.*, 1987, **22**, p 1135-1140.

6. C.L. Yeh and G.T. Liou, Effects of PTFE Activation and Excess Al on Combustion Synthesis of SiC- and ZrC-Al$_2$O$_3$ Composites, *Vacuum*, 2018, **154**, p 186-189.

7. A. Mirabi, M. Sharifitabar and M. Shafiee Afarani, Self-propagating High-Temperature Synthesis of (Zr, W)C/WC/Al$_2$O$_3$ Composite Powders from WO$_3$-ZrO$_2$-Al-C System, *Int. J. Refract. Met. Heat Meter.*, 2019, **82**, p 279-286.

8. C. Huo, L. Guo, L. Zhou, B. Liu, C. Wang, Y. Zhang and H. Wang, Effect of Al$_2$O$_3$ Addition on the Ablation Behavior of SiC-ZrC Coated C/C Composites, *J. Alloy Compd.*, 2018, **752**, p 489-504.

9. R. Aliasgarian, M. Naderi and S.E. Mirsalehi, Ablation Mechanism of ZrB$_2$-SiC Coating for SiC-Coated Graphite Under an Oxyacetylene Flame, *Surf. Coat. Tech.*, 2018, **350**, p 511-518.

10. D.-J. Yao, H.-J. Li, H. Wu, Q.-G. Fu and X.-F. Qiang, Ablation Resistance of ZrC/SiC Gradient Coating for SiC-Coated Carbon/Carbon Composites Prepared by Supersonic Plasma Spraying, *J. Eur. Ceram. Soc.*, 2016, **36**, p 3739-3746.

11. T. Liu, Y. Niu, C. Li, J. Zhao, J. Zhang, Y. Zeng, X. Zheng and C. Ding, Effect of MoSi$_2$ Addition on Ablation Behavior of ZrC Coating Fabricated by Vacuum Plasma Spray, *Ceram. Int.*, 2018, **44**, p 8946-8954.

12. L. Zhou, Q. Fu, C. Huo, Y. Wang and M. Tong, A Novel Oxidation Protective SiC-ZrB$_2$-ZrSi$_2$ Coating with Mosaic Structure for Carbon/Carbon Composites, *Ceram. Int.*, 2018, **44**, p 14781-14788.

13. C. Huo, L. Zhou, L. Guo, J. Wang, Y. Li, J. Sun and L. Liu, Effect of the Al$_2$O$_3$ Additive on the High Temperature Ablation Behavior of the ZrC-ZrO$_2$ Coating for SiC-Coated Carbon/Carbon Composites, *Ceram. Int.*, 2019, **45**, p 23180-23195.

14. K. Wang, L. Chen, C. Xu, W. Zhang, Z. Liu, Y. Wang, J. Ouyang, X. Zhang, Y. Fu and Y. Zhou, Microstructure and Mechanical Properties of (TiZrNbTaMo)C High-Entropy Ceramic, *J. Mater. Sci. Technol.*, 2020, **39**, p 99-105.

15. L. Wang, L. Si, Y. Zhu and Y. Qian, Solid-State Reaction Synthesis of ZrC from Zirconium Oxide at Low Temperature, *Int. J. Refract. Met. Heat Meter.*, 2013, **38**, p 134-136.

16. X. Zhu, Y. Zhang, H. Li, J. Zhang, Y. Fu and Y. Su, SiC/SiC-ZrSi$_2$ Coating with Micro-Pore to Protect C/C Composites Against Oxidation for Long-Life Service at High Temperatures, *Corros. Sci.*, 2021, **191**, p 109780.

17. H. Richard and J. Hannink, Transformation Toughening in Zirconia-Containing Ceramics, *J. Am. Ceram. Soc.*, 2000, **83**, p 461-487.

18. T. Chraska, K. Neufuss, J. Dubský, P. Ctibor and P. Rohan, Fabrication of Bulk Nanocrystalline Alumina-Zirconia Materials, *Ceram. Int.*, 2008, **34**, p 1229-1236.

19. L. Xu, C. Huang, H. Liu, B. Zou, H. Zhu, G. Zhao and J. Wang, Study on the Synthesis and Growth Mechanisms of the Refractory ZrC Whiskers, *Int. J. Refract. Met. Heat Meter.*, 2014, **42**, p 116-119.

20. M. Mahdavi, M. Ramazani and Z. Darvishi, Synthesis and Characterization of Zirconium Carbide Nanorods at Low Temperature, *Int. J. Refract. Met. Heat Meter.*, 2016, **56**, p 59-62.

21. Q. Liu, L. Zhang, L. Cheng and Y. Wang, Chemical Vapour Deposition of Zirconium Carbide and Silicon Carbide Hybrid Whiskers, *Mater. Lett.*, 2010, **64**, p 552-554.

22. K. Li, X. Zhou, Z. Zhao, C. Chen, C. Wang, B. Ren and L. Zhang, Synthesis of Zirconium Carbide Whiskers by a Combination of Microwave Hydrothermal and Carbothermal Reduction, *J. Solid State Chem.*, 2018, **258**, p 383-390.

23. X. Zhang, B. Zhang, M. He, Z. Yang, Y. Su and K. Wu, Microstructure and Mechanical Properties of In-Situ Synthesized (ZrC + Er$_2$O$_3$+ ZrCr$_2$)/Zr Composite Prepared by Arc-Melting, *Mater. Des.*, 2015, **88**, p 619-624.

24. J.D. Jarman, W.G. Fahrenholtz, G.E. Hilmas, J.L. Watts and D.S. King, Characterization of Fusion Welded Ceramics in the SiC-ZrB$_2$-ZrC System, *J. Eur. Ceram. Soc.*, 2021, **41**, p 2255-2262.

25. S. Yao, C. Li, J. Tian, G. Yang and C. Li, Conditions and Mechanisms for the Bonding of a Molten Ceramic Droplet to a Substrate after High-Speed Impact, *Acta Mater.*, 2016, **119**, p 9-25.

26. S. Yao, C. Li, G. Yang and C. Li, Influence of Microstructure on the Mechanical Integrity of Plasma-Sprayed TiO$_2$ Splat, *J. Eur. Ceram. Soc.*, 2017, **37**, p 4979-4989.

27. J. Xu, B. Zou, S. Zhao, S. Hui, W. Huang, X. Zhou, Y. Wang, X. Cai and X. Cao, Fabrication and Properties of ZrC–ZrB$_2$/Ni Cermet Coatings on a Magnesium Alloy by Atmospheric Plasma Spraying of SHS Powders, *Ceram. Int.*, 2014, **40**, p 15537-15544.

28. X. Fan, W. Huang, X. Zhou and B. Zou, Preparation and Characterization of NiAl-TiC-TiB$_2$ Intermetallic Matrix Composite Coatings by Atmospheric Plasma Spraying of SHS Powders, *Ceram. Int.*, 2020, **46**, p 10512-10520.

29. J. Shen, B. Zou, S. Dong, X. Cai and X. Cao, Fabrication and Characterization of TiB$_2$-TiC-Co Wear-Resistant Coatings on AZ91D Magnesium Alloy, *Surf. Coat. Tech.*, 2019, **364**, p 358-368.

30. D. Hong, Y. Niu, H. Li, X. Zhong, W. Tu, X. Zheng and J. Sun, Comparison of Microstructure and Tribological Properties of Plasma-Sprayed TiN, TiC and TiB$_2$ Coatings, *Surf. Coat. Tech.*, 2019, **374**, p 181-188.

31. X. Sun, W. Li, J. Huang, Z. Ye, J. Yang, S. Chen and X. Zhao, Effect of Si Content on the Microstructure and Properties of Ti-Si-C Composite Coatings Prepared by Reactive Plasma Spraying, *Ceram. Int.*, 2021, **47**, p 24438-24452.

32. Y. Cui, Y. Guo, Y. Shao, Y. Yang, Y. Ma, W. Sun, Y. Dong and D. Yan, Effects of SiC on Microstructure and Properties of Plasma Sprayed ZrB$_2$-ZrC Composite Coating, *Ceram. Int.*, 2021, **47**, p 12753-12761.

33. Y. Cui, Q. Zhang, Y. Shao, Y. Yang, Y. Ma, W. Sun, Y. Wang, X. Wang and Y. Dong, Microstructure and Properties of In-Situ ZrB$_2$-ZrC Composite Coatings by Plasma Spraying, *Surf. Coat. Tech.*, 2021, **409**, p 126846.

34. F. Sajedi Alvar, M. Heydari, A. Kazemzadeh, M.R. Vaezi and L. Nikzad, Synthesis and Characterization of Corrosion-Resistant and Biocompatible Al$_2$O$_3$-TiB$_2$ Nanocomposite Films on Pure Titanium, *Ceram. Int.*, 2020, **46**, p 4215-4221.

35. L. Yuan, P. Zhang, F. Zuo, R. Luo, Z. Guo, K. Plucknett, B. Jiang, G. Nie, F. Meng, V. Valcárcel-Juárez, A. Maître and H.-T. Lin, Comparison of Sintering Behavior and Reinforcing Mechanisms Between 3Y-TZP/Al$_2$O$_3$(w) and 12Ce-TZP/Al$_2$O$_3$ (w) Composites: Combined Effects of Lanthanide Stabilizer and Al$_2$O$_3$ Whisker Length, *J. Eur. Ceram. Soc.*, 2021, **41**, p 706-718.